Journal of
Materials Chemistry C

PAPER

View Article Online
View Journal | View Issue

Cite this: J. Mater. Chem. C, 2016, 4, 10664

Angular-dependent magnetism in Co(001) single-crystal nanowires: capturing the vortex nucleation fields

A. H. Montazer,*[a] A. Ramazani,[ab] M. Almasi Kashi[ab] and J. Zavašnik[c]

Experimental realization of analytically predicted behavior for nanoscale magnetic systems can pave the way for promoting synergistic research and has significant importance for applications and thorough understanding of nanomagnetism. Here, we report on the magnetism of a nearly ideal nanowire (NW) system, vertically aligned hcp-Co(001) single-crystal NWs electrochemically deposited inside an aluminum oxide template, as a function of the angle ($0^\circ \le \theta \le 90^\circ$) between the magnetic field and the NW axis. Using high resolution transmission electron microscopy, detailed structural investigations on the few micrometers long and approximately 45 nm in diameter NWs exhibit crystalline inhomogeneities at the NW ends, evidencing magnetic localization in the single crystalline NWs. Using a vibrating sample magnetometer enabled us to extract different magnetic parameters, thereby evaluating angular dependence of magnetism in NW arrays and individual NWs. While the conventional hysteresis and first-order reversal curve (FORC) diagram methods show a monotonic decreasing and increasing behavior for coercivity as a function of θ, respectively, the average coercivity obtained from the irreversible distribution indicates a non-monotonic behavior, involving a complex magnetization reversal triggered by the propagation of vortex domain walls (DWs) and single vortex states for high field angles. Additionally, the hysteresis curve coercivity is phenomenologically parameterized at each θ based on the angular FORC (AFORC) measurements. Comparing the AFORC coercivities (varying between 5 kOe at $\theta = 0^\circ$ and 9.3 kOe at $\theta = 90^\circ$) with absolute values of the angular dependence of the vortex nucleation field confirms an almost complete concurrence between experimental findings and analytical calculations on individual NWs. Consequently, our results show the first analytically supported evidence on capturing the nucleation fields and the occurrence of vortex DW propagation at each θ for weakly interacting Co NW arrays with a large magnetocrystalline anisotropy along the length.

Received 26th August 2016,
Accepted 11th October 2016

DOI: 10.1039/c6tc03697j

www.rsc.org/MaterialsC

Introduction

The efficient control of low dimensional magnetic systems, including nanowires (NWs), has spurred research towards the understanding and tuning of magnetization processes, thereby realizing their future applications in patterned magnetic media, data processing and spintronic devices.[1–3] As a breakthrough in this research area, magnetic NW arrays have been considered for 3 dimensional racetrack memory, storing information by utilizing domain walls (DWs) with magnetic vortices.[4–6] Being pertinent to the aforementioned applications, magnetic anisotropy has a pivotal role in determining magnetic properties.[7,8] For NWs, magnetic anisotropy mainly originates from the contribution of shape anisotropy (SA) and magnetocrystalline anisotropy (MCA). The MCA in a single crystal is defined as the energy that is required to rotate the magnetic moment from an easy to a hard crystalline axis, arising from the interaction between the magnetic moment of spin and the crystal lattice.[9]

While most of the early studies on magnetic NWs were focused on exploratory investigations such as inducing an easy axis by the SA, recent research subjects have shifted toward the understanding of angular-dependent properties, involving both SA and MCA.[10–12] In most cases, however, the aforementioned anisotropies compete with each other, making it difficult to reveal the effective magnetic contribution.[11,13,14] Ideally, SA and MCA would be aligned along the same axis, thereby reinforcing each other. This could be realized in large-aspect-ratio (>10) cylindrical NWs with a uniaxial MCA parallel to the long axis. In the case of hexagonal close-packed (hcp) structures (*e.g.*, Co),

[a] Institute of Nanoscience and Nanotechnology, University of Kashan, P. O. Box: 87317–51167, Kashan, Iran. E-mail: montazer.a@grad.kashanu.ac.ir, amirh.montazer@gmail.com; Fax: +98 3155912895; Tel: +98 9132775935
[b] Department of Physics, University of Kashan, Kashan 87317-51167, Iran
[c] Centre for Electron Microscopy and Microanalysis (CEMM), Jožef Stefan Institute, Ljubljana, Slovenia

the easy axis can be uniaxial, giving rise to a large MCA along the NW length. For single crystalline hcp-Co NWs, this MCA easy axis is along the [001] direction.[12] Therefore, large-aspect-ratio hcp-Co(001) single-crystal NWs could be an ideal model system in which to investigate the emerging angular dependence of magnetism, providing insights into the magnetization processes and magnetic properties. Under such conditions, the magnetic properties would appear to be very sensitive to the angle between the applied field and the NW axis (θ), based upon the literature.[12,15–17] Consequently, it is necessary to tune the angle for the subsequent investigations. In this regard, using a solid template-based method for the fabrication of NWs enables us to have vertically aligned NWs by which the magnetic field angle can be precisely controlled with respect to the NW axis. In particular, compared to the track-etched polycarbonate templates with irregularities (*e.g.*, crossed nanopores), the anodic aluminum oxide templates provide arrays of well-defined cylindrical nanopores with tunable aspect-ratios.[7] Therefore, in terms of angle-dependent measurements, vertically aligned NWs electrochemically deposited into anodic aluminum oxide templates are much more applicable compared to randomly dispersed NWs made of chemical solution methods,[18,19] thereby leading to reliable magnetic results.

With regard to the recent magnetic trend, the angular dependence of magnetism can be experimentally obtained for NW arrays and individual NWs based on the conventional hysteresis curve measurements and advanced approaches including the first-order reversal curve (FORC), magneto-optical Kerr effect (MOKE) and magnetic force microscopy (MFM).[11,15,17,20,21]

The conventional approach is the magnetic response averaged over an enormous number of NWs, resulting in a major hysteresis curve with single coercivity and remanence ratio characterizations. On the other hand, the MOKE and MFM measurements can provide magnetic results on individual NWs in terms of switching field, median coercivity and magnetization reversal mode.[11,17,22] However, when it comes to angular measurements, the resolution of both methods is limited up to certain angles ($\theta < 70^\circ$).[17,20]

Moreover, surface features cause variations in the MFM contrast and oxidation may influence the MOKE signal, requiring further investigations.[11,17] Notably, using the MOKE method on individual pure Co and NiCo with different compositions, recent statistical magnetometry resulted in uncertain and poor statistics when increasing the perpendicular MCA of Co.[11] In other words, the large MCA constant of Co (K_{MCA} = 4.5 × 10^6 erg cm^{-3}) perpendicular to the NW axis induces a large reversible switching component, making subtle magnetic effects hard to characterize *via* MOKE measurements. In turn, this creates curvilinear hysterons instead of basic hysterons with irreversible magnetization processes for the clear-cut properties of individual NWs in device design applications.[11,17,23,24] In this way, the most promising alternative approach to overcome these hurdles is the use of the FORC diagram method.[23,25–28]

Apart from the ease of fine-tuning the field angle for the vertically aligned NW arrays, the FORC method is capable of providing the distribution of switching fields for NWs with different individual properties. Additionally, the FORC diagrams of NWs manifest the irreversible switching field as a single peak (H_c^{FORC}), approximating to the MOKE switching field and/or nucleation field, particularly for weak interactions and low MCA perpendicular to the NW axis.[11] Therefore, H_c^{FORC} may represent the nucleation/switching field of individual NWs, which is experimentally challenging to obtain due to the very small magnetization of single NWs (in the order of 10^{-11} emu).[28,29] This can also be applicable for unraveling complicated mechanisms when the NWs reverse their magnetization.[30] However, FORC diagrams show only irreversible switching events; in other words, reversible magnetization cannot make any contribution to a FORC diagram. In particular, this can be observed when changing θ, since the anisotropic magnetic system comprised of NWs is expected to behave as an ideal Stoner–Wohlfarth hysteron, making no hysteric event at $\theta = 90^\circ$ (*i.e.*, a 100% reversible component).[31] In this concept, FORC measurements can quantitatively determine the irreversible and reversible component fractions by evaluating the difference between magnetization of the major hysteresis curve and minor FORCs.[32] As a result, the angular dependence of irreversible hysteresis curves extracted from the FORC measurements can represent the average response of irreversible events, as discussed by Winklhofer *et al.*[32]

There is currently a great deal of FORC investigation on different types of magnetic NWs reported in the literature, describing their magnetic states, magnetic phases, coercivity and magnetostatic interaction distributions and so forth.[33–35] However, they have mostly focused on the parallel ($\theta = 0^\circ$) and perpendicular ($\theta = 90^\circ$) FORC diagrams. In the case of polycrystalline Co NWs without a preferential MCA, the angular FORC (AFORC) diagrams indicate complex magnetic behaviors when $0^\circ \leq \theta \leq 90^\circ$.[15,36] In this regard, while H_c^{FORC} remained almost constant as a function of θ, the angular-dependent distributions of coercivity and interactions were examined to determine the magnetization reversal process in the polycrystalline Co NWs.[15]

In this paper, we have been able to fabricate vertically aligned hcp-Co(001) single-crystal NWs using an electrochemical deposition technique. The resulting cylindrical NWs embedded inside an anodic aluminum oxide template are approximately 45 nm in diameter and a few micrometers in length. These single crystalline NWs with large MCA (parallel to the NW axis) and weak interactions are considered as a nearly ideal nanoscale magnetic system, enabling the careful study of angular dependence of magnetism. This is experimentally realized based on conventional and advanced magnetometry using major hysteresis curve and AFORC analyses, respectively.

Experimental details

The anodic aluminum oxide template was prepared using the well-known two-step anodization method in oxalic acid.[37] In this respect, a high purity aluminum disk (99.999%) was ultrasonically degreased in acetone and subsequently electropolished (at 4 °C in a mixed solution of ethanol and perchloric acid; 4 : 1 in volume) for 3.5 min using a current density of approximately 100 mA cm^{-2}. At 17 °C, the first step was performed in 0.3 M oxalic acid for 5 h using a potential of 40 V. The anodized layer was then etched away in a mixed solution of phosphoric acid and chromic acid at 60 °C for 5 h. With the same parameters as those of the first step, the second anodization was carried out for 3 h, inducing highly ordered nanopores with a length of approximately 30 μm, a diameter of 30 nm and an inter-pore distance of 100 nm.[38] With a pore-widening process in 0.3 M phosphoric acid at 30 °C, the diameter of the pores was increased to approximately 45 nm. Prior to performing a pulsed electrochemical deposition inside the nanopores, the anodization potential was exponentially decreased from 40 to 10 V in order to promote the thinning of the insulating barrier layer of alumina.

Co NW arrays were electrochemically grown inside the template using a pulsed deposition with optimized fabrication parameters and electrolyte conditions. The fabrication parameters included the sine pulse-shape with reduction/oxidation potentials of 12/10 V, a pulse time of 3.2 ms with a delay-time of 37 ms between pulses, a cathodic current density peak of approximately 30 mA cm^{-2} and a deposition charge of 3C. The electrolyte conditions included 0.3 M $CoSO_4 \cdot 7H_2O$ with 0.73 M H_3BO_3 and a pH of 5.20 at 30 °C under constant stirring. The remaining aluminum of the template and a piece of graphite served as the working and counter electrodes, respectively. Under these conditions, 10 μm long cylindrical NW arrays with a diameter of approximately 45 nm are synthesized, as will be characterized later.

After performing the electrochemical process, the remaining aluminum of the NW sample was etched in a solution of $CuCl_2$ for a few minutes. Then, at 30 °C, the alumina barrier layer was removed using 0.3 M phosphoric acid for 40 min, as schematically illustrated elsewhere.[39] Since the initial growth of the electrodeposited NWs has been shown to follow a transition from polycrystal to single crystal,[40,41] the length of the Co NWs was progressively reduced enough (in the order from bottom to top) to remove the polycrystalline parts, most likely leading to a development in the crystallinity of the remaining NWs. This chemical etching was carried out using 0.3 M phosphoric acid at 30 °C for approximately 120 min. At this stage, the resulting NWs were a few micrometers in length, as will be shown later.

The morphological properties of the alumina template and the resulting NWs were studied using a field-emission scanning electron microscope (FE-SEM; MIRA3 TESCAN) and a 200 kV LaB_6 transmission electron microscope (TEM; JEOL JEM-2100). The crystalline properties were studied using X-ray diffraction (XRD, Philips X'Pert Pro; Cu Kα radiation; λ = 0.154 nm) and TEM techniques utilizing structure-dependent electron scattering: selected area electron diffraction (SAED) and dark-field TEM (DF-TEM) imaging.

The angular dependence of magnetism was studied using a vibrating sample magnetometer (VSM; MDKB, Iran) at room temperature. In this respect, the angular hysteresis curves and AFORC diagrams of vertically aligned NWs were investigated for $0^\circ \leq \theta \leq 90^\circ$. At each θ, the AFORC diagrams were obtained by applying a positive magnetic field H, in order to saturate the NW sample. Thereafter, the applied field H was reduced to a reversal field H_r. The magnetization curve $M(H,H_r)$ was measured, which resulted in a minor FORC when increasing H back to the positive saturation. The FORC distribution of FORC(ρ) is given by:[26]

$$\rho(H, H_r) = -\frac{1}{2}\frac{\partial^2 M(H, H_r)}{\partial H \partial H_r} \tag{1}$$

For each diagram, the coercive field (H_c) and interaction field (H_u) distributions are represented as a counter plot with a color scale from blue to red, corresponding to the minimum and maximum FORC distributions, respectively. Furthermore, H_c and H_u axes are defined as: $H_c = (H - H_r)/2$ and $H_u = (H + H_r)/2$. In this way, the maximum peak position of coercivity along the H_c axis ($H_{c,max}^{FORC}$) was extracted from the AFORC diagrams. Moreover, the irreversible and reversible components of magnetization were identified from the AFORC measurements. The irreversible change is the difference between the major hysteresis curve and FORC magnetizations, given by eqn (2):[32]

$$dM^{Irrev.} = \lim_{H \to H_r}[M(H) - M(H, H_r)] \tag{2}$$

The reversible change is given below:

$$dM^{Rev} = \lim_{H \to H_r}[M(H, H_r) - M(H_r)] \tag{3}$$

In this way, in addition to calculating the magnetization components, irreversible and reversible hysteresis curves were reconstructed from the FORC measurements.[32] The coercivity of the irreversible hysteresis curve was then extracted, indicating the average value of the irreversible FORC distribution along the H_c axis ($H_{c,avg}^{FORC}$).

Results and discussion

As elaborated in the experimental details, the Co NWs were initially pulse-electrodeposited inside the anodic aluminum oxide template under optimized conditions. Using chemical etching, the length of the NWs was then reduced (from bottom to top) to eliminate polycrystalline parts. The morphological and crystalline properties, and angular dependence of magnetism were studied, as will be presented and discussed in the following sections.

A. Morphological and crystalline properties

Fig. 1(a) shows a TEM micrograph of the anodic aluminum oxide template with well-aligned nanopore channels and a diameter of approximately 45 nm. The high resolution TEM (HR-TEM) micrograph together with the corresponding experimental and rotationally averaged SAED ring-patterns in Fig. 1(b) demonstrates randomly oriented crystal grains from the alumina template, with grains up to 10–20 nm in size. On the other hand, Fig. 1(c) shows the FE-SEM image of the as-fabricated 10 μm long Co NW arrays embedded in the alumina template with a thickness of approximately 30 μm. The inset in Fig. 1(c) depicts the FE-SEM image of the Co NWs with reduced lengths (a few micrometers in length) after their release from the template. The XRD pattern of these NWs is shown in Fig. 1(d).

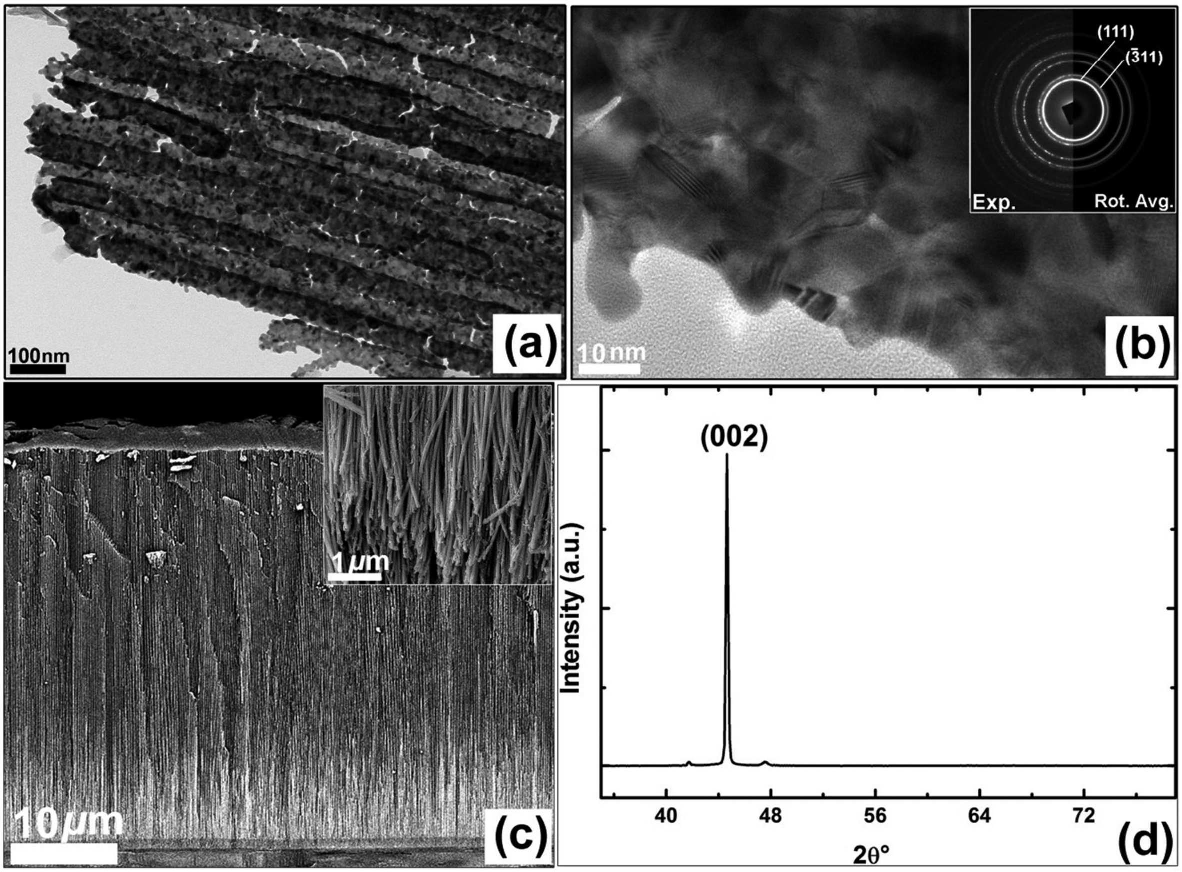

Fig. 1 (a) TEM and (b) HR-TEM micrographs of the anodic aluminum oxide template. The top-right inset in part (b) is the corresponding experimental and rotationally averaged SAED patterns. (c) FE-SEM image of the as-fabricated Co NW arrays embedded inside the anodic aluminum oxide template. The top-right inset in part (c) is the FE-SEM image of the Co NWs with reduced lengths after their release from the template. (d) XRD pattern of vertically aligned Co NWs after reducing their length.

This indicates the fabrication of vertically aligned hcp-Co NW arrays with a single crystal structure oriented along the [001] direction after further processing. Notably, using the Scherrer equation, the crystallite size is found to be about 40 nm, approximating to the NW diameter.

Note that the minor peaks detected at $2\theta \approx 41.6^\circ$ and 47.5° can be attributed to the Co(100) and (101) planes, respectively.[12] To obtain complementary information on the crystalline properties of individual NWs, the HR-TEM and DF-TEM micrographs accompanied with the SAED patterns of single Co NWs were obtained and the results are presented in Fig. 2. As observed in Fig. 2(a), the corresponding SAED pattern of the Co NW shows a high quality hcp-Co single-crystal structure so that the growth direction is along the [001] direction. In turn, this indicates the hcp-(001) *c*-axis parallel to the NW axis, leading to a large MCA along the NW length at a diameter of about 45 nm. Note that the blurred rings in the SAED pattern of the Co NW correspond to the polycrystalline structure of the alumina template (the remaining residue), as can be inferred from the SAED patterns inserted in Fig. 1(b). The HR-TEM micrograph of the single Co NW accompanied with the fast Fourier transform (FFT) pattern (the top-left inset in Fig. 2(b)) exhibit parallel fringes along the NW length with a lattice spacing of *ca.* 0.41 nm, corresponding to the (002) plane of Co. On the other hand, the crystalline characteristics of a single Co "NW end" are shown in Fig. 2(c and d). While the DF-TEM micrograph obtained from the NW end (see Fig. 2(d)) demonstrates a single crystalline section with a length of 170 nm, the corresponding SAED pattern (the inset of Fig. 2(c)) shows a less developed hcp-crystalline structure. This is associated with the presence of diffraction spots originating from neighboring crystals with a deflected orientation of up to 60° along the NW length. In this respect, the insets in Fig. 2(d) graphically depict the crystalline phase analysis, evidencing the overlapping of crystallographic planes with the growth direction of [001] at the NW end. This may give rise to random MCA effects at the NW ends, which in turn can influence the resulting properties.[42,43] Altogether, the resulting hcp-Co NWs are found to be single crystalline with a growth direction along the [001], indicating the *c*-axis parallel to the long axis of the NWs.

B. Angular dependence of magnetism

The angular-dependent magnetism of the vertically aligned Co(001) single-crystal NWs was studied and compared based on the different magnetometry described in the experimental details. The results obtained are presented in Fig. 3–5. Fig. 3(a) shows the corresponding angular major hysteresis curves

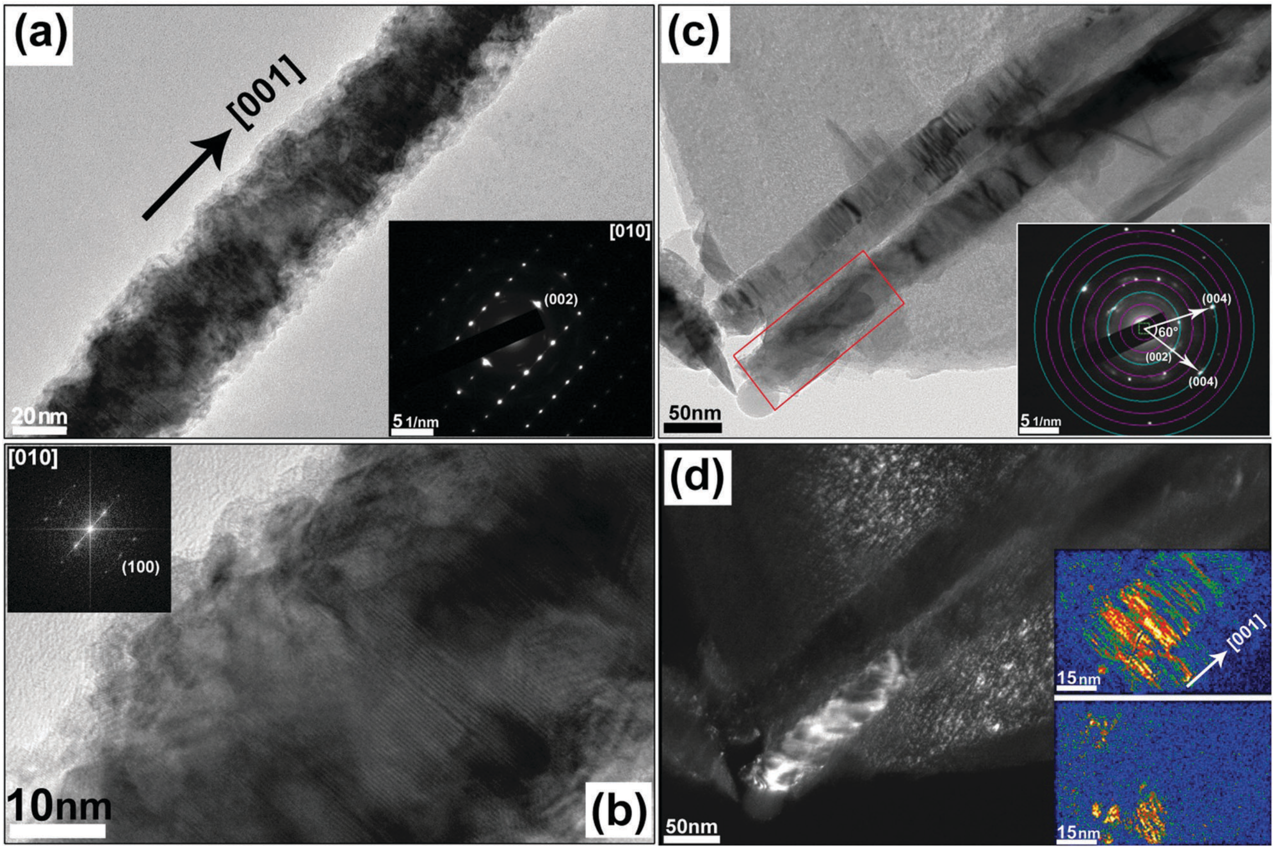

Fig. 2 (a) TEM and (b) HR-TEM micrographs of a Co(001) single-crystal NW. The insets in parts (a) and (b) correspond to the SAED and FFT patterns along the NW length, respectively. (c) TEM micrograph of single Co NWs, marking the NW end associated with the corresponding SAED pattern. (d) DF-TEM micrograph of the single NW in part (c). The insets in part (d) graphically depict the crystalline phase analysis of a single Co NW end.

for $0^\circ \leq \theta \leq 90^\circ$. This highlights the narrowing of the square curve, followed by the continual decrease in the major hysteresis curve coercivity (H_c^{Hyst}) between 5 kOe and 0.65 kOe when increasing θ from 0° to 90°.

On the other hand, part (b) in Fig. 3 shows the angular irreversible hysteresis curves reconstructed from the AFORC measurements for $0^\circ \leq \theta \leq 90^\circ$, featuring both the coercivity and the reversible component (the solid and dotted arrows, respectively). As seen, the square curve at $\theta = 0^\circ$ is almost a perfect irreversible curve (*i.e.*, with a reversible component of approximately 0%) whereas at $\theta = 90^\circ$, the corresponding curve is nearly reversible (with a component of about 98%).

In the case of the ideal hcp-Co NWs with a growth direction of [001], the angle between the *c*-axis and NW axis is zero, indicating a large MCA along the length. Therefore, from an initial evaluation of the angular-dependent behavior of the Co NWs, a nearly coherent rotation might be considered, particularly at $\theta = 90^\circ$ with the reversible switching. Taking into account the Stoner–Wohlfarth model for a perfect coherent rotation of magnetization, the total anisotropy field (H_k) is the sum of the MCA and SA fields. In the case of bulk Co, the MCA field is found to be 7.6 kOe at room temperature whereas the SA field, H_{SA}, for a prolate ellipsoid can be obtained as follows:[44]

$$H_{SA} = J_s(N_x - N_z) \qquad (4)$$

where $J_s = 4\pi M_s$, in which M_s is the saturation magnetization, N_x and N_z are the perpendicular and parallel demagnetizing factors with respect to the long axis of the ellipsoid, respectively. An infinitely long ellipsoid is the approximation to a single component cylindrical NW with high-aspect-ratio (>10), for which the N_x and N_z are found to be 1/2 and 0, respectively.[31]

In this way, H_k for an individual Co NW with a uniaxial MCA will be the sum of 7.6 kOe and 8.8 kOe (*i.e.*, H_{SA} with M_s = 1400 emu cm^{-3}) when the magnetic field is applied parallel to the NW axis. Disregarding the magnetic interactions and the NW diameter, this magnetic anisotropy field prediction up to 16.4 kOe theoretically defines the upper limit of the coercivity for Co NWs at room temperature, which has been challenging to achieve.[44,45] In other words, the experimental coercive field values are usually much weaker than H_k due to random anisotropy effects, giving rise to a competition between the magnetic anisotropy and exchange energies.[9,42] This may involve localized and/or non-coherent magnetization reversal processes as well, extending throughout the NWs.

In fact, even in single crystalline NWs, these effects are induced by the structural and geometrical features such as impurities, structural defects and irregular morphologies, particularly along the length and at the NW ends,[42,46] as also evidenced in this study (see Fig. 2(c and d)). These deficiencies may cause a small part of the NW to be magnetically softer than

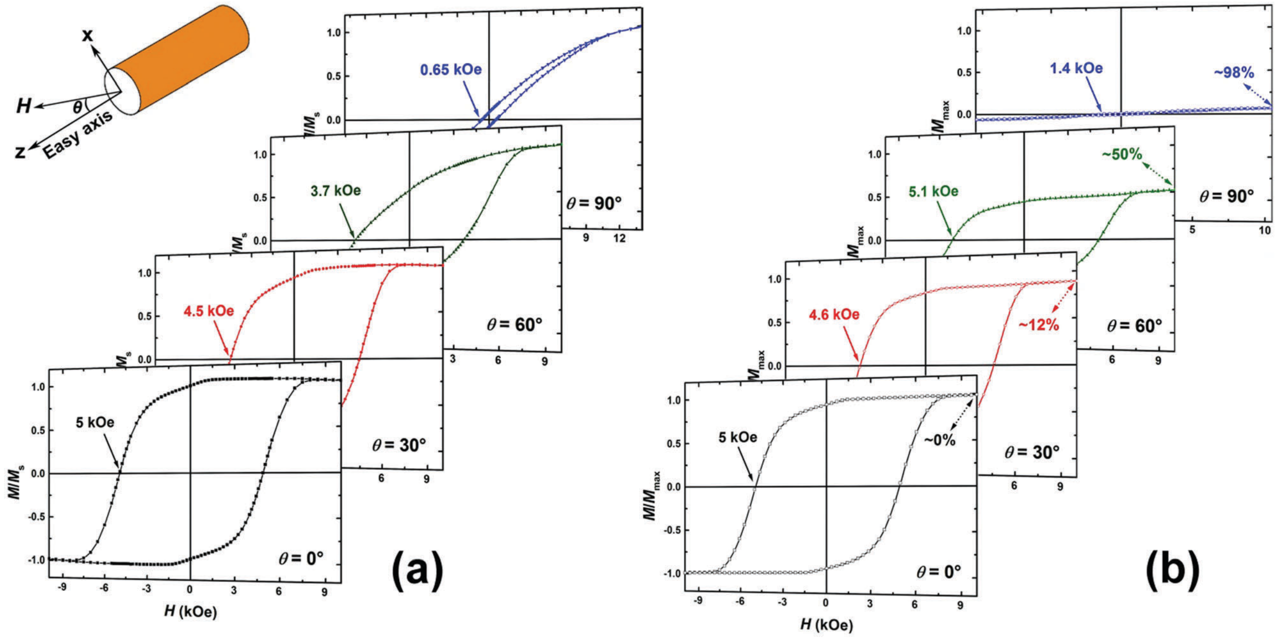

Fig. 3 (a) Angular dependence of the major hysteresis curves and (b) angular dependence of the irreversible hysteresis curves for Co(001) single-crystal NW arrays when $0^\circ \leq \theta \leq 90^\circ$. The top-left inset schematically illustrates the magnetic field angle θ with respect to the NW axis (the easy axis). M_s in part (a) is the saturation magnetization and M_{max} in part (b) is the maximum magnetization of the major hysteresis curve. The solid arrows in parts (a) and (b) show the coercive field position and the dotted arrows in part (b) indicate the reversible components.

the remaining part of the NW.[42] Therefore, under these conditions, the localization of magnetization could occur, followed by a decrease in the coercivity compared to H_k. Phenomenologically, the experimental coercivity can be expressed according to eqn (5):[47]

$$H_c = \alpha\frac{2K_u}{M_s} - N_{eff}M_s \tag{5}$$

where α is a crystallite orientation – and reversal mode – dependent parameter, K_u is the uniaxial anisotropy constant and N_{eff} is an effective demagnetizing factor justifying the magnetostatic interactions. Thereby, the optimized values of experimental coercivity for advanced magnetic systems are obtained to be 30–40% of H_k.[9]

With the above considerations, the coercivity of 5 kOe at $\theta = 0^\circ$ for the single crystalline Co NWs with the *c*-axis parallel to the NW axis could be rationalized in terms of experimental optimization, making them a nearly ideal model NW system. This high coercivity value is further understood by comparing it to the coercivities in this diameter range reported in the literature (<2 kOe).[47,48] It is important to emphasize that, in principle, a uniform rotation by the coherent mode in magnetic NWs is realized at diameters smaller than the coherent diameter (D_{Coh}), as given below:[47]

$$D_{Coh} = 7.31\sqrt{\frac{A}{4\pi M_s^2}} \tag{6}$$

where A is the exchange stiffness constant. Taking $A \approx 1.8 \times 10^{-6}$ erg cm^{-1}, D_{Coh} for Co NWs is found to be about 19 nm. As a result, the emerging reversal modes in magnetic NWs including those triggered by DW movement should be taken into consideration when evaluating the magnetization reversal in the Co(001) single-crystal NWs with a diameter of 45 nm.[12,13,21] In this respect, micromagnetic simulations proposed by Ivanov *et al.* on single crystalline Co NWs with diameters up to 50 nm showed that nucleation and propagation of DWs are responsible for the magnetization reversal at $\theta = 0^\circ$.[21] However, apart from the presence of vortex states at the NW ends in the remanent state, the reversal mode remained the same when increasing θ in the range $0^\circ < \theta < 90^\circ$.[13,21] Alternatively, at $\theta = 90^\circ$, the reversal mode changed from vortex and/or transverse DW to a quasi-coherent rotation mode based on the micromagnetic investigations.[21]

As mentioned earlier, the AFORC diagram method can be employed to experimentally extract the magnetization reversal process.[15] Here, angular-dependent magnetism of the hcp-Co NWs with a parallel *c*-axis (thus representing a nearly ideal experimental system) was investigated using AFORC diagrams when $0^\circ \leq \theta \leq 90^\circ$, as can be observed in Fig. 4(a–i). The quantitative results of the different magnetometry as a function of θ have also been compared and summarized in Fig. 5(a and b).

Fig. 4(a) shows a nearly symmetric FORC distribution with a sharp peak along the H_c axis ($H_{c,max}^{FORC}$) at $\theta = 0^\circ$. This also exhibits weakly interacting NWs as evidenced from the narrow distributions with a low FORC density along the H_u axis. At this stage, H_c^{Hyst}, $H_{c,max}^{FORC}$ and $H_{c,avg}^{FORC}$ result in almost the same value ($\approx$5 kOe) due to the nearly perfect irreversible magnetization component at $\theta = 0^\circ$ (*i.e.*, a reversibility of *ca.* 0%; see Fig. 3(b) and 5(b)). Furthermore, the occurrence of the high coercivity (H_c^{Hyst} = 5 kOe at $\theta = 0^\circ$) in the Co(001) NWs with a large MCA might be attributed to a magnetization reversal mechanism by the nucleation

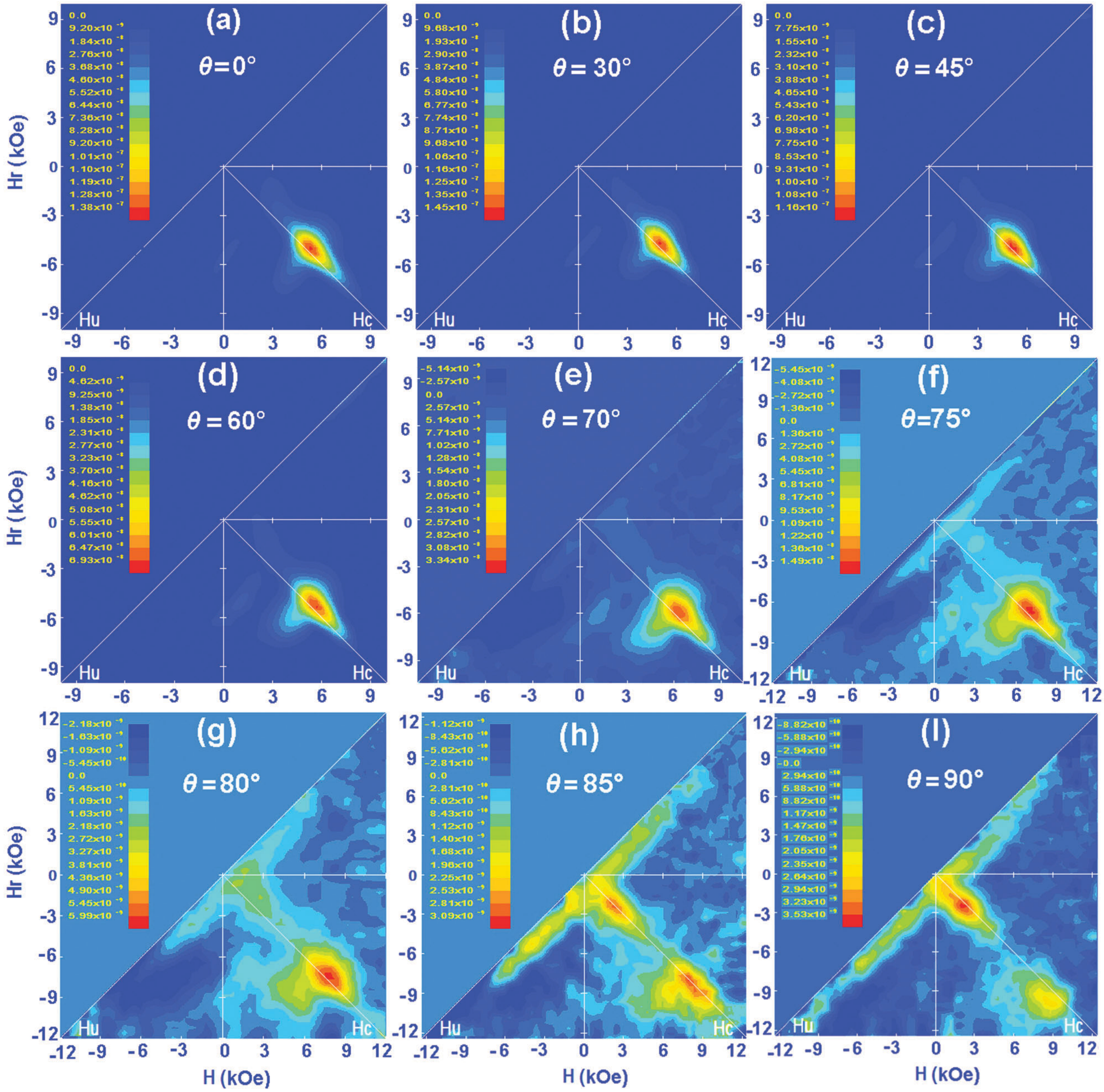

Fig. 4 AFORC diagrams of Co(001) single-crystal NW arrays for (a) θ = 0°, (b) θ = 30°, (c) θ = 45°, (d) θ = 60°, (e) θ = 70°, (f) θ = 75°, (g) θ = 80°, (h) θ = 85° and (i) θ = 90°. Note the different magnitude of the external magnetic field *H*.

and propagation of vortex DW, as previously predicted by Vivas *et al.*[12] for [001]-textured Co NWs with a diameter of 50 nm and a length of a few micrometers.

While increasing θ from 0° to 45° increases the reversible component up to 25%, there are no considerable differences in the shape of the AFORC diagrams and/or between $H_{c,max}^{FORC}$ and $H_{c,avg}^{FORC}$. In fact, the irreversible events have remained almost the same during the magnetization reversal for 0° $\leq \theta \leq$ 45° due to the strong alignment of the *c*-axis with the NW axis. Nevertheless, as can be seen in Fig. 5(a and b), the reversible switching has influenced the H_c^{Hyst} and remanence ratio (M_r/M_s), thereby decreasing them from 5 to 4.2 kOe and 0.97 to 0.73, respectively. With a similar FORC distribution shape, increasing θ up to 60° significantly increases the reversible component to 50%, because of which $H_{c,max}^{FORC}$ and $H_{c,avg}^{FORC}$ increase up to 5.4 kOe and 5.1 kOe, whereas H_c^{Hyst} and M_r/M_s decrease to 3.7 kOe and 0.53, respectively. As a result, the enhancement in the reversibility efficiently contributes to the major hysteresis curve characteristics. This follows the general experimental behavior of the angular dependence of coercivity and remanence in magnetic Co NWs.[12,21] At θ = 70°, a low density positive coercive field region (ranging between 450 and 2600 Oe) is observed near the origin of the corresponding AFORC diagram (see Fig. 4(e)), indicating the addition of an irreversible switching mechanism with a small coercivity. Moreover, a negative feature in the lower quadrant of the diagram starts to appear, arising

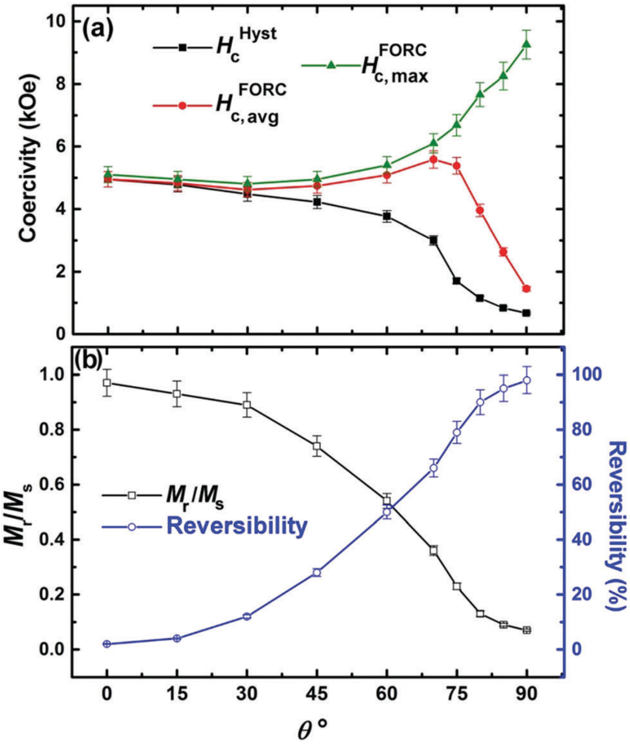

Fig. 5 The comparison between the angular-dependent magnetism of Co(001) single-crystal NW arrays based on the major hysteresis curve, AFORC diagram and irreversible hysteresis curve measurements: (a) coercivity and (b) M_r/M_s and reversibility, as a function of θ.

from the coupling between the irreversible and reversible magnetization components as discussed elsewhere.[49] Concomitantly, however, both $H_{c,max}^{FORC}$ and $H_{c,avg}^{FORC}$ are enhanced up to 20% and 10%, respectively, compared to $\theta = 0°$. As a consequence, the newly emerged irreversible features have contributed to the decrease of H_c^{Hyst} (to 3 kOe) and less developing $H_{c,avg}^{FORC}$ (as compared to $H_{c,max}^{FORC}$) in the wake of the reversible component of 65% (see Fig. 5(b)).

In continuance, the variation behavior of $H_{c,max}^{FORC}$ remains similar, whereas H_c^{Hyst} significantly decreases to 1.6 kOe, followed by a reversible component of 80% when increasing θ by only 5° (θ = 75°). In turn, this results in a decrease in $H_{c,avg}^{FORC}$, as can also be evidenced from the noticeable FORC distribution of the low coercivity region, according to Fig. 4(f). In other words, while $H_{c,max}^{FORC}$ and H_c^{Hyst} follow their analytically predicted behavior (based on the nucleation field of vortex DW)[12] and experimentally observed variation as a function of θ,[21] respectively, $H_{c,avg}^{FORC}$ can provide better insights into the complex angular-dependent magnetism behavior of the Co(001) single-crystal NW arrays. Furthermore, $H_{c,max}^{FORC}$ appears to be an interesting experimental parameter to explore the nucleation/switching field of individual NWs for each θ. This will be discussed in detail later.

Thus, for $\theta > 70°$, the decrease in $H_{c,avg}^{FORC}$ is indicative of the increasing development in the irreversible low coercivity region around the origin of the diagram, accompanied by an enhancement in the reversibility up to 98% and a decrease in M_r/M_s to 0.07 at θ = 90°. For clarity, we have defined $\delta(\theta) = H_{c,avg}^{FORC} - H_c^{Hyst}$ and $\delta'(\theta) = H_{c,max}^{FORC} - H_{c,avg}^{FORC}$ for $0° \leq \theta \leq 90°$, as shown in Fig. 6(a). As inferred, $\delta(\theta)$ indicates the significant increase in the reversibility ($45° < \theta \leq 75°$) and the development of the low coercivity region ($75° < \theta \leq 90°$). On the other hand, $\delta'(\theta)$ demonstrates the perfect irreversible evolution of the magnetization reversal induced by the propagation of the vortex DW, in particular, for $\theta > 70°$. Now, we can also define $\phi(\theta) = H_c^{Hyst} - H_{c,avg}^{FORC}$, in order to examine the concept of average coercivity at each θ and see whether it is possible to find a new way of calculating the hysteresis curve coercivity based on the AFORC measurements. $\phi(\theta)$ for each θ is shown in Fig. 6(b), indicating a monotonic decreasing behavior ($0.29 \leq \phi(\theta) \leq 1$) when $0° \leq \theta \leq 80°$. Coincidentally, the corresponding irreversibility (*i.e.*, 1 − reversibility fraction) is found to be between 0.98 and 0.10 for $0° \leq \theta \leq 80°$, as shown in Fig. 6(b).

As a result, $\phi(\theta)$ and irreversibility follow each other in terms of variation fraction (between 1 and 0), although they differ when $\theta > 80°$. The correlation of $\phi(\theta)$ with irreversibility leads us to compare H_c^{Hyst} and $H_{c,avg}^{FORC} \times$ Irrev., according to Fig. 7(a). Interestingly, although the corresponding values do not coincide with each other, the variation behavior is nearly the same. Importantly, this phenomenologically provides the relationship

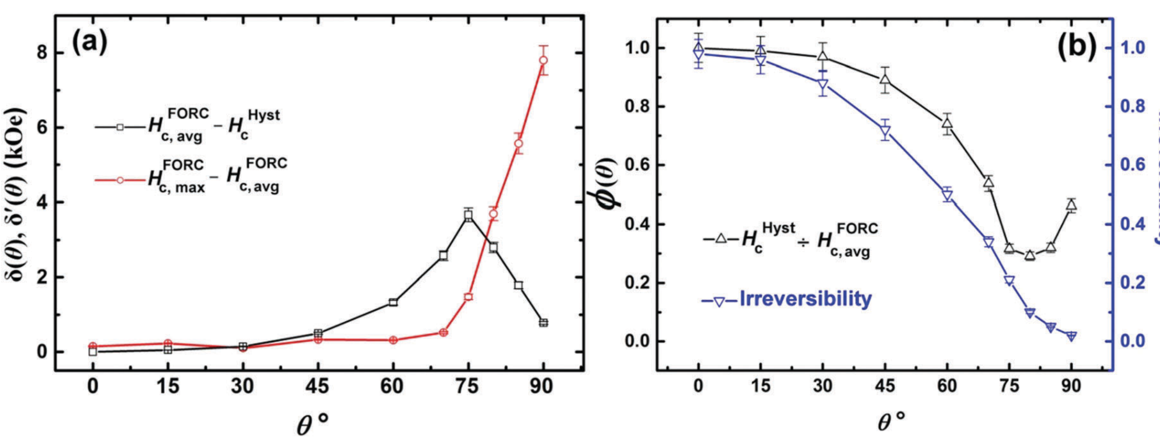

Fig. 6 (a) $\delta(\theta)$ and $\delta'(\theta)$; (b) $\phi(\theta)$ and irreversibility; extracted from the angular hysteresis curves and AFORC measurements.

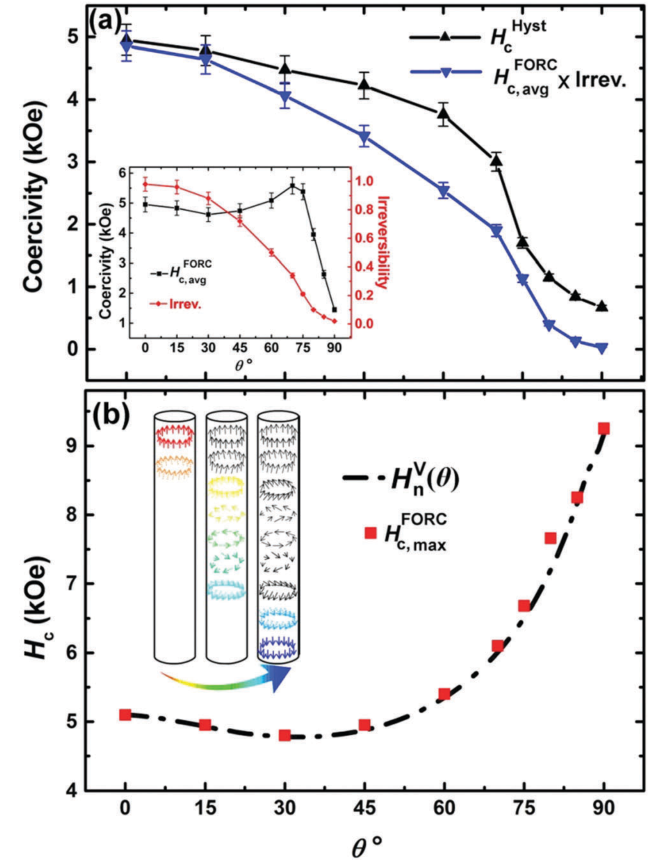

Fig. 7 (a) The comparison between coercivities, H_c^{Hyst} and $H_{c,avg}^{FORC} \times$ Irrev.; the inset shows the $H_{c,avg}^{FORC}$ and irreversibility as a function of θ. (b) The comparison between the FORC data ($H_{c,max}^{FORC}$) and the analytical calculations ($H_n^V(\theta)$) on the angular dependence of nucleation field of vortex DW in the Co(001) single-crystal NW arrays and a single Co NW, respectively. The inset in part (b) is a schematic representation of the magnetization reversal by the vortex mode, in which the arrows depict the orientation of magnetic moments inside the single NW.

between the angular dependence of coercivity (*i.e.*, $H_c^{Hyst}(\theta)$ from the hysteresis curve method) and the angular dependence of irreversible coercivity distribution (*i.e.*, $H_{c,avg}^{FORC}$ from the AFORC measurements) as expressed below:

$$H_c^{Hyst}(\theta) = \beta \times \text{Irrev.}(\theta) \times H_{c,avg}^{FORC}(\theta) \tag{7}$$

where β may be a magnetization reversal mode-dependent parameter. As seen in Fig. 6(b), the behavior of $\phi(\theta)$ and the irreversibility is different when $\theta > 80°$. Essentially, the perceptible low coercivity distributions with a FORC peak at 2.2 kOe (prominently for $\theta > 80°$) may be attributed to a combined magnetization reversal by vortex and single vortex (SV) states with broad nucleation/annihilation fields.[50,51] Therefore, in addition to the vortex DW mode evidenced by the continual increase in $H_{c,max}^{FORC}$ up to approximately 9.3 kOe at $\theta = 90°$ (Fig. 4(i) and 5(a)), the combined vortex states with low coercivity distributions are efficient in decreasing H_c^{Hyst} and $H_{c,avg}^{FORC}$ to 0.65 kOe and 1.4 kOe, respectively. The complexity of the magnetization reversal might then be reflected in the parameter β as θ increases, thereby deflecting H_c^{Hyst}. Note that, all the switching distributions depicted in Fig. 4(i) result from the irreversible magnetization component by a fraction of about 0.02. Thus, there might be switching events, which would not be necessarily detectable in the AFORC diagrams.

Note also that, using experimental findings assisted with analytical solutions, previous investigations on polycrystalline Co NWs have assumed a perfect transition between vortex and transverse DWs when increasing θ ($<90°$), evidenced by the non-monotonic behavior of H_c^{Hyst} and/or abrupt increase in the FORC distribution.[15,52] Herein, the AFORC diagram method assisted with the irreversible/reversible component fractions has enabled us to reveal the subtle differences in the complex switching behavior of the magnetization at each θ for single crystalline Co NWs.

In fact, with the *c*-axis parallel to the NW axis, the changes in the reversibility as a function of θ are credible in interpreting and precisely extracting the angular dependence of magnetism. For this reason, the irreversible switching of the vortex DW follows its predicted behavior based on the analytical methods. In this regard, $H_{c,max}^{FORC}$ may quantitatively provide information on the nucleation field of the DWs, which has been an important challenge to be obtained experimentally. As a proof of concept, we have performed extended analytical calculations of the angular dependence of nucleation field based on the vortex DW mode, $H_n^V(\theta)$, as given below:[53]

$$H_n^V(\theta)\cos(\theta - \gamma) = \{N_x(L)\sin^2(\gamma) + N_z(L)\cos^2(\gamma) - C - D[3\cos^2(\gamma) - 1]\}M_s \tag{8}$$

$$H_n^V(\theta)\sin(\theta - \gamma) = \left\{[N_x(L) - N_z(L) + D]\left(\frac{\sin(2\gamma)}{2}\right)\right\}M_s \tag{9}$$

where $C = \dfrac{q^2 {L_{ex}}^2}{R^2}$ and $D = \dfrac{K_{MCA}}{{M_s}^2}$ in which R is the NW radius; L_{ex} is the exchange length and γ is the angle at which the nucleation starts. In the case of a cylindrical geometry, $q^2 = 1.08\pi$.[53] Therefore, to obtain $H_n^V(\theta)$, we simultaneously solved eqn (8) and (9) for each applied field angle after taking $L_{ex} = 3.8$ nm and $M_s = 1400$ emu cm^{-3}. The best agreement with experimental points was obtained using $K_{MCA} \approx 0.2 \times 10^6$ erg cm^{-3}. The results for the $H_n^V(\theta)$ were compared with the $H_{c,max}^{FORC}$, as presented in Fig. 7(b).

As inferred, apart from the same variation behavior, the absolute values calculated for the nucleation field are very similar to those of $H_{c,max}^{FORC}$ when $0° \leq \theta \leq 90°$. This indicates a significant agreement between the FORC data and the theoretical prediction on the angular dependence of the nucleation field of vortex DW in an individual Co NW and the Co(001) single-crystal NW arrays, respectively.

Considering the previous literature reports on the comparison between the analytical computations and experimental measurements using angular dependence of coercivity,[12,52,53] the almost complete concurrence between H_n^V and $H_{c,max}^{FORC}$ at each θ has no precedent for Co and Co-based magnetic NW systems (especially when $\theta > 60°$). Since the general trend of H_c^{Hyst} in the NW arrays with aspect ratios >10 is to show a decreasing behavior (at high field angles) due to the shape anisotropy reduction, experimental efforts have been unable to provide credible evidences for the occurrence of the magnetization reversal by the propagation of vortex DW.[15,52]

Indeed, in 1997, Aharoni[54] initially calculated the angular dependence of the nucleation field in an ellipsoid for a magnetization reversal triggered by a curling rotation, which is similar to the vortex DW mode if within a finite volume.[21] In this case, an abrupt change in the magnetization of the individual system could take place at or near the vortex nucleation field.[53] This concept was then extended to evaluate the magnetization reversal mechanism in cylindrical NW arrays by fitting of analytical calculations to experimental points (obtained from the angular dependence of coercivity using major hysteresis curve measurements). In other words, the angular dependence of the coercivity (H_c^{Hyst}) was assumed to be a close approximation to that of the nucleation field of the vortex mode H_c^V in which it constantly increases with increasing θ.[12,21] Therefore, extracting $H_{c,max}^{FORC}$ from the AFORC diagrams enables us to capture the nucleation/switching field of individual single crystalline Co NWs with a large MCA along the NW length, realizing clear experimental evidences for the analytical model predictions. It should be noted that the previous studies have ascribed the overestimations of the calculated coercivity values to the magnetostatic interactions between the NW arrays,[12,55] as was expressed in eqn (5). Here, the AFORC distributions along the H_u axis of the highly coercive region show the weak magnetostatic interactions involved in the magnetization reversal process. For this reason, N_{eff} may be ignored, thereby realizing the nearly ideal magnetic NW system.

Summary and conclusions

Nearly ideal Co single-crystal NWs (*ca.* 45 nm in diameter with a growth direction of [001]) were fabricated using electrochemical deposition inside an aluminum oxide template, thereby providing vertically aligned arrays. This enabled us to precisely investigate the angular-dependent magnetism of Co NWs with a large MCA along the length using major hysteresis curve, irreversible hysteresis curve and AFORC diagram methods assisted with analytical computations for $0^\circ \leq \theta \leq 90^\circ$. The TEM analysis (including HR-TEM, SAED and DF-TEM) on individual NWs revealed the presence of structural defects such as the overlapping of crystallographic planes in the single crystalline NWs, especially at the NW ends. This may justify the overestimation of H_k ($\approx$16.4 kOe) compared to the optimized experimental coercivity ($\approx$5 kOe), thus inducing a localized nucleation field and magnetization reversal by non-coherent rotation modes. Extracting the corresponding coercivities from the aforementioned magnetometry, H_c^{Hyst}, $H_{c,max}^{FORC}$ and $H_{c,avg}^{FORC}$ provided complementary information on the magnetization reversal mechanisms in NW arrays and individual NWs. In this way, we phenomenologically expressed the relationship (eqn (7)) by which to calculate H_c^{Hyst} at each θ, originating from the average magnetic response of irreversible coercivity distributions.

When $\theta < 45^\circ$, the magnetometry parameters resulted in similar values, indicating that the magnetic field angle can be safely ignored in the resulting magnetism, followed by the reversible magnetization component of up to 25%. For $45^\circ < \theta \leq 90^\circ$, $H_{c,avg}^{FORC}$ provided better insights into the complex angular-dependent magnetism behavior of the Co(001) single-crystal NW arrays, comprising a combined magnetization reversal by the propagation of vortex DWs and SV states, prominently when $\theta > 80^\circ$. On the other hand, $H_{c,max}^{FORC}$ increased up to 85% when increasing θ between 0° and 90°, realizing experimental evidences on the vortex nucleation fields as compared with the analytical method. The remanence ratio followed the irreversible magnetization component as reduced from 0.97 to 0.07 with decreasing irreversibility from approximately 0.98 to 0.02. Moreover, AFORC diagrams showed the weak magnetostatic interactions involved in the magnetization reversal process. These results may invigorate experimentalists to provide ideal model magnetic NW systems in which to investigate magnetism and find applications, while also encouraging theorists to make vigorous predictions about the corresponding nanoscale behavior.

Acknowledgements

The authors thank the University of Kashan for providing the financial support for this work by Grant No. 159023/47.

References

1 X. Kou, X. Fan, R. K. Dumas, Q. Lu, Y. Zhang, H. Zhu, X. Zhang, K. Liu and J. Q. Xiao, *Adv. Mater.*, 2011, **23**, 1393–1397.
2 M. Gavagnin, H. D. Wanzenboeck, S. Wachter, M. M. Shawrav, A. Persson, K. Gunnarsson, P. Svedlindh, M. Stöger-Pollach and E. Bertagnolli, *ACS Appl. Mater. Interfaces*, 2014, **6**, 20254–20260.
3 J.-M. Hu, T. Yang, K. Momeni, X. Cheng, L. Chen, S. Lei, S. Zhang, S. Trolier-McKinstry, V. Gopalan and G. P. Carman, *Nano Lett.*, 2016, **16**, 2341–2348.
4 S. S. Parkin, M. Hayashi and L. Thomas, *Science*, 2008, **320**, 190–194.
5 S. Parkin and S.-H. Yang, *Nat. Nanotechnol.*, 2015, **10**, 195–198.
6 Y. P. Ivanov, A. Chuvilin, S. Lopatin and J. Kosel, *ACS Nano*, 2016, **10**, 5326–5332.
7 E. Araujo, A. Encinas, Y. Velázquez-Galván, J. M. Martínez-Huerta, G. Hamoir, E. Ferain and L. Piraux, *Nanoscale*, 2015, **7**, 1485–1490.
8 J. García, V. Vega, L. Iglesias, V. M. Prida, B. Hernando, E. D. Barriga-Castro, R. Mendoza-Reséndez, C. Luna, D. Görlitz and K. Nielsch, *Phys. Status Solidi A*, 2014, **211**, 1041–1047.
9 D. J. Sellmyer and R. Skomski, *Advanced magnetic nanostructures*, Springer Science & Business Media, 2006.
10 M. S. Arshad, S. Šturm, J. Zavašnik, A. P. Espejo, J. Escrig, M. Komelj, P. J. McGuiness, S. Kobe and K. Ž. Rožman, *J. Nanopart. Res.*, 2014, **16**, 1–16.
11 P. Sergelius, J. G. Fernandez, S. Martens, M. Zocher, T. Böhnert, V. V. Martinez, V. M. de la Prida, D. Görlitz and K. Nielsch, *J. Phys. D: Appl. Phys.*, 2016, **49**, 145005.

12 L. Vivas, J. Escrig, D. Trabada, G. Badini-Confalonieri and M. Vázquez, *Appl. Phys. Lett.*, 2012, **100**, 252405.
13 L. Vivas, Y. P. Ivanov, D. Trabada, M. Proenca, O. Chubykalo-Fesenko and M. Vázquez, *Nanotechnology*, 2013, **24**, 105703.
14 C. Bran, Y. P. Ivanov, D. Trabada, J. Tomkowicz, R. del Real, O. Chubykalo-Fesenko and M. Vazquez, *IEEE Trans. Magn.*, 2013, **49**, 4491–4497.
15 M. Proenca, J. Ventura, C. Sousa, M. Vazquez and J. Araujo, *J. Phys.: Condens. Matter*, 2014, **26**, 116004.
16 C. Bran, A. Espejo, E. Palmero, J. Escrig and M. Vázquez, *J. Magn. Magn. Mater.*, 2015, **396**, 327–332.
17 E. V. Vidal, Y. P. Ivanov, H. Mohammed and J. Kosel, *Appl. Phys. Lett.*, 2015, **106**, 032403.
18 W. Fang, I. Panagiotopoulos, F. Ott, F. Boué, K. Ait-Atmane, J.-Y. Piquemal, G. Viau and F. Dalmas, *J. Nanopart. Res.*, 2014, **16**, 1–10.
19 M. Gong, Q. Dai and S. Ren, *Nanotechnology*, 2016, **27**, 07LT02.
20 E. M. Palmero, C. Bran, R. P. del Real and M. Vázquez, *Nanotechnology*, 2015, **26**, 461001.
21 Y. P. Ivanov, M. Vázquez and O. Chubykalo-Fesenko, *J. Phys. D: Appl. Phys.*, 2013, **46**, 485001.
22 M. Tabasum, F. Zighem, J. D. L. T. Medina, A. Encinas, L. Piraux and B. Nysten, *J. Appl. Phys.*, 2013, **113**, 183908.
23 C. Pike, *Phys. Rev. B: Condens. Matter Mater. Phys.*, 2003, **68**, 104424.
24 N. Lei, T. Devolder, G. Agnus, P. Aubert, L. Daniel, J.-V. Kim, W. Zhao, T. Trypiniotis, R. P. Cowburn and C. Chappert, *Nat. Commun.*, 2013, **4**, 1378.
25 C.-I. Dobrotă and A. Stancu, *Physica B*, 2015, **457**, 280–286.
26 C. Pike, C. Ross, R. Scalettar and G. Zimanyi, *Phys. Rev. B: Condens. Matter Mater. Phys.*, 2005, **71**, 134407.
27 C.-I. Dobrotă and A. Stancu, *J. Appl. Phys.*, 2013, **113**, 043928.
28 F. Béron, A. Yelon, D. Ménard and L.-P. Carignan, *Extracting individual properties from global behaviour: first-order reversal curve method applied to magnetic nanowire arrays*, INTECH, 2010.
29 M. S. Sultan and D. Atkinson, *Mater. Res. Express*, 2016, **3**, 056104.
30 K. Pirota, F. Béron, D. Zanchet, T. Rocha, D. Navas, J. Torrejón, M. Vazquez and M. Knobel, *J. Appl. Phys.*, 2011, **109**, 083919.
31 L. Sun, Y. Hao, C.-L. Chien and P. C. Searson, *IBM J. Res. Dev.*, 2005, **49**, 79–102.
32 M. Winklhofer, R. K. Dumas and K. Liu, *J. Appl. Phys.*, 2008, **103**, 07C518.
33 M. Ciureanu, F. Béron, P. Ciureanu, R. Cochrane, D. Ménard, A. Sklyuyev and A. Yelon, *J. Nanosci. Nanotechnol.*, 2008, **8**, 5725–5732.
34 T. R. F. Peixoto and D. R. Cornejo, *J. Magn. Magn. Mater.*, 2008, **320**, e279–e282.
35 R. Lavin, J. C. Denardin, J. Escrig, D. Altbir, A. Cortes and H. Gomez, *IEEE Trans. Magn.*, 2008, **44**, 2808–2811.
36 E. Jafari-Khamse, M. A. Kashi and A. Ramazani, *Mater. Chem. Phys.*, 2015, **159**, 128–138.
37 H. Masuda and K. Fukuda, *Science*, 1995, **268**, 1466.
38 A. Ramazani, V. Asgari, A. H. Montazer and M. A. Kashi, *Curr. Appl. Phys.*, 2015, **15**, 819–828.
39 S. Samanifar, M. A. Kashi, A. Ramazani and M. Alikhani, *J. Magn. Magn. Mater.*, 2015, **378**, 73–83.
40 X. Huang, G. Li, G. Sun, X. Dou, L. Li and L. Zheng, *Nanoscale Res. Lett.*, 2010, **5**, 1057.
41 X. Huang, L. Li, X. Luo, X. Zhu and G. Li, *J. Phys. Chem. C*, 2008, **112**, 1468–1472.
42 R. Skomski, H. Zeng, M. Zheng and D. J. Sellmyer, *Phys. Rev. B: Condens. Matter Mater. Phys.*, 2000, **62**, 3900.
43 J. Cantu-Valle, I. Betancourt, J. E. Sanchez, F. Ruiz-Zepeda, M. M. Maqableh, F. Mendoza-Santoyo, B. J. Stadler and A. Ponce, *J. Appl. Phys.*, 2015, **118**, 024302.
44 K. Gandha, K. Elkins, N. Poudyal, X. Liu and J. P. Liu, *Sci. Rep.*, 2014, **4**, 5345.
45 K. Soulantica, F. Wetz, J. Maynadié, A. Falqui, R. Tan, T. Blon, B. Chaudret and M. Respaud, *Appl. Phys. Lett.*, 2009, **95**, 152504.
46 M. Viqueira, G. Pozo-López, S. Urreta, A. Condó, D. Cornejo and L. Fabietti, *J. Appl. Phys.*, 2015, **117**, 204301.
47 D. J. Sellmyer, M. Zheng and R. Skomski, *J. Phys.: Condens. Matter*, 2001, **13**, R433.
48 L. Cattaneo, S. Franz, F. Albertini, P. Ranzieri, A. Vicenzo, M. Bestetti and P. Cavallotti, *Electrochim. Acta*, 2012, **85**, 57–65.
49 I. Bodale, L. Stoleriu and A. Stancu, *IEEE Trans. Magn.*, 2011, **47**, 192–197.
50 R. K. Dumas, C.-P. Li, I. V. Roshchin, I. K. Schuller and K. Liu, *Phys. Rev. B: Condens. Matter Mater. Phys.*, 2007, **75**, 134405.
51 R. K. Dumas, T. Gredig, C.-P. Li, I. K. Schuller and K. Liu, *Phys. Rev. B: Condens. Matter Mater. Phys.*, 2009, **80**, 014416.
52 M. Proenca, C. Sousa, J. Escrig, J. Ventura, M. Vazquez and J. Araujo, *J. Appl. Phys.*, 2013, **113**, 093907.
53 L. Vivas, M. Vazquez, J. Escrig, S. Allende, D. Altbir, D. Leitao and J. Araujo, *Phys. Rev. B: Condens. Matter Mater. Phys.*, 2012, **85**, 035439.
54 A. Aharoni, *J. Appl. Phys.*, 1997, **82**, 1281–1287.
55 R. Lavin, J. C. Denardin, J. Escrig, D. Altbir, A. Cortés and H. Gómez, *J. Appl. Phys.*, 2009, **106**, 103903.

